Cadmium Selective Etching in CdTe Solar Cells Produces Detrimental Narrow-gap Te in Grain Boundaries

Sudhajit Misra[1], Jeffery A. Aguiar[2], Sophia Gardner[3], Xiahan Sang[4], Raymond R. Unocic[4], Amit Munshi[5], Walajabad S. Sampath[5], Chris S. Ferekides[6], and Michael A. Scarpulla[1,3]*

[1] Department of Electrical and Computer Engineering, University of Utah, 50 S. Central Campus Dr., MEB Rm 2110, Salt Lake City, Utah 84112, USA

[2] Nuclear Materials Department, Idaho National Laboratory, 2525 Fremont Ave., MS 3870, Idaho Falls, ID, 83415, USA.

[3] Department of Materials Science and Engineering, University of Utah, Salt Lake City, UT, 84102, USA

[4] Center for Nanophase Materials Science, Oak Ridge National Laboratory, 1 Bethel Valley Rd., Oak Ridge, TN, 37830, USA.

[5] Department of Mechanical Engineering, Colorado State University, Fort Collins, CO 80523, USA

[6] Department of Electrical Engineering, University of South Florida, Mail Point: ENB118, 4202 East Fowler Ave, Tampa, FL 33620, USA

.

KEYWORDS: polycrystalline CdTe, thin-film solar cell, grain boundary, wet etching, aberration-corrected STEM, electron energy loss spectroscopy

ABSTRACT:

Recent advances in design and processing technology have made possible commercialization of polycrystalline (px-) CdTe as a photovoltaic absorber. Grain boundaries (GBs) are the most prominent structural defects in these devices and undergo significant changes during device fabrication. However, the effects of device fabrication processes on these GBs are not entirely understood. Prevailing models of GBs in thin-film photovoltaics consider individual GBs to have homogeneous properties in their area. Here, using an aberration-corrected scanning transmission electron microscope (STEM) -based low-loss and core-loss electron energy loss spectroscopy (EELS), we show that back-surface etching of CdTe leads to inhomogeneity within individual grain boundaries. We observe that etching the back surface leads to the conversion of a region of GBs from CdTe to an elemental Te, which has an only 0.33 eV bandgap, as deep as 1 μm from the back surface. The presence of elemental Te in GBs this deep into the absorber layer will increase recombination in the absorber layer and limit the extractable open-circuit voltage, thus reducing device efficiency. However, additive methods for back contact formation such as deposition of Te, ZnTe, or other materials preserve the CdTe stoichiometry of the GBs. Thus, especially for the next generations of CdTe-based cells having longer minority carrier diffusion length and/or thinner absorber layers, additive back contacting methods are superior.

ONE SENTENCE SUMMARY:

We demonstrate using low-loss and core-loss electron energy loss spectroscopy that etching the back surface of CdTe solar cells to create a Te surface layer also leads to elemental Te in the near-surface region of grain boundaries, demonstrate that deposition of Te layers does not, and

discuss the harmful effects of having narrow-gap Te in grain boundaries especially in next-generations of devices.

INTRODUCTION:

Solar cells of polycrystalline CdTe are the leading commercialized thin-film photovoltaic (TFPV) technology for utility-scale electricity generation. CdTe was the first PV technology to achieve manufacturing costs below $1/Wp (earlier than even Si), thus ushering in the current era of PV proliferation. The high absorption coefficient (>10^5 /cm) for photon energies above its 1.5 eV bandgap allows CdTe absorber layers only a few μm thick to absorb its usable portion of the solar spectrum completely. CdTe cell efficiencies greater than 22% and module efficiencies greater than 18% have been reported.[1,2] However, a significant gap still exists between these efficiencies and CdTe's maximum theoretical efficiency of ~32%.[1,3] Increasing the open-circuit voltage (V_{OC}) to over 1 V by increasing lifetime and doping are the current crucial challenges for pushing CdTe device efficiency over 25%. However, high V_{OC} cannot be achieved only by improving absorber doping and lifetime - reducing the interface recombination velocities at the front and back interfaces will become more and more vital as minority carrier diffusion length increases.[4–6]

Rapid improvements in CdTe TFPV efficiency were achieved in the last decade, primarily by improving short-circuit current density (J_{SC}). These improvements in J_{SC} were achieved by replacing the conventional CdS n-type buffer layer with a broader gap buffer layers and by alloying CdTe with Se near the front junction to reduce the bandgap by approximately 100 meV.[7–10] Very recently, the additional roles of Se in improving intragrain lifetime as well as helping to passivate grain boundaries have been elucidated.[11–13] As the technology moves

towards 25% efficiency and V_{OC} approaches greater than 1 V, increases in bulk minority carrier lifetimes and higher doping will allow thinner cells. Thus, in the near future, any mechanism causing either non-radiative recombination or radiative recombination in a lower bandgap phase (as we describe herein) at or near the back contact will continue to rise towards the top of the Pareto list of factors limiting V_{OC}.

Grain boundaries (GBs) are the most prominent structural defects in CdTe thin-films after the nearly ubiquitous $CdCl_2$ treatment, which largely removes stacking faults and twin boundaries. Charged grain boundaries and their associated potential result in a high density of midgap states in the bandgap (10^{11}-10^{12} /cm^3 required to produce higher than 50 mV potential for grains with typical doping higher than 10^{15} /cm^3), as opposed to being caused by shallow dopant states. Such intra-gap charge transition levels will participate in defect-assisted recombination and generation. The effects of vertical (through-thickness) GBs have been computationally explored; in forward bias, GBs result in increased recombination at their intersection with the nominally-planar junction depletion width increasing $J_o(V)$ [14–22]. A helpful device physics insight is that the GB potential only exists in the quasineutral region. Within the main junction depletion width, the intragap GB states behave as recombination-generation centers just as they would if uniformly distributed. Thus, despite widespread discussion of beneficial effects GB potentials separating photocarriers and increasing $J_{light}(V)$ near J_{SC}, unless the GB states have zero recombination activity, the increased $J_o(V)$ in forward bais outweighs such supposed benefits and always reduces photovoltaic conversion efficiency. The best passivated GBs in CdTe to date is still estimated to have recombination velocity higher than 10^4 cm/s. Summarizing, charged vertical GBs may be beneficial for polycrystalline thin-film photodetectors or radiation detectors

operated in zero to reverse bias but are unequivocally deleterious to thin-film photovoltaics operated in forward bias.

The existing literature has assumed the structure and properties of GBs to be homogeneous across their surface area. GBs are generally classified in terms of their coincident site lattice character. While this description is sufficient to distinguish individual grains, it is insufficient to describe their interfacial atomic arrangement and thus their electronic structure.[15,17,22–27] Our past work on laser annealing of the CdTe back surface and our work on the investigation of GB chemistry near the back contact have demonstrated chemical inhomogeneity within a GB.[28,29] These investigations have opened an avenue of exploration in TFPV on the variation in GB properties with position along their surface and its implications on device physics. Especially given historical low-doping in CdTe grains and the propensity of surfaces and interfaces to form intra-gap states, the formation of Ohmic contacts has been challenging and led to efficiency losses. A widely-practiced historical approach has been to etch the back surface to form an elemental Te layer before deposition of a metallic back contact.[30–36] More recent approaches have deposited doped ZnTe or Te to aid in the ohmic back contact formation.[37,38] Additionally, chemical etching is the preferred method to create a Te back layer in solution-deposited and flexible CdTe TFPV devices.[39–42] Within 1D slab-on-slab device physics analysis, these approaches should be equivalent. We have shown here that the presence of GBs makes etching and additive deposition processes inequivalent to CdTe TFPV performance.

Understanding the effects of etching on the chemical composition, electronic structure, and valence states of the GB region are quite challenging and require the latest innovations in high-resolution valence electron energy loss spectroscopy (V-EELS).[43,44] Combining the spatial and energy resolution involves using aberration-corrected scanning transmission electron microscopy

(STEM) and V-EELS to correlate physical defects and structure with local changes in atomic bonding and configuration below the core loss regime.[45,46] While core-loss electron energy-loss spectroscopy (CL-EELS) provides element-specific electronic structure information with limited energy resolution, overlapping edges, plasmonic features, and spurious X-ray signals make extraction of such information more complex below ~150 eV, in the valence regime.[45] V-EELS enables spatially-resolved detection of bandgaps and the broadening at near edge joint density of states just above the Fermi energy in semiconductors, which in principle includes measurements of bandgap and the dielectric response of the bulk.

Herein, we present first-of-its-kind direct evidence from high-resolution transmission electron microscope-based core- and valence- EELS data that commonly-used etching processes used to prepare a Cd-poor layer for improved Ohmic back contacts results in phase transformation of 1.5 eV CdTe to a smaller bandgap, 0.33 eV, Te along GBs near their intersection with the back surface. We utilized core-loss EELS to measure compositional changes and low-loss (valence) EELS to characterize phases present. Elemental spatial chemical composition extracted from core-loss EELS is correlated with valence EELS spectral imaging to reveal a direct relation between elemental chemical composition and low lying energy loss features, which are indicative of changes in electronic bandstructure.[47,48] Kramers-Kronig (KK) analysis and electron density functional theory (DFT) is used to reveal trends in the measurable differences in the electronic states and relate it to dielectric properties. KK analysis reveals the spatially coordinated complex dielectric function. We have compared and integrated high-resolution imaging and spectroscopy to reveal the underlying origins associated with Cd depletion and Te enrichment in Br:MeOH etched px-CdTe TFPV devices. Additionally, we show that additive back contact processes such as deposition of Te or ZnTe layers, which to our

knowledge are used, at least coincidentally, in all cells to date exhibiting AM1.5 efficiencies above 17%, do not induce such phase changes. Our study is also potentially applicable to other thin-film material applications where chemical etching is used to modify or change the surface chemistry.[49–51]

RESULTS AND DISCUSSION:

The CdTe electron-transparent lamella lift outs (thinned to approximately 60-100 nm) were characterized using STEM and EELS in both the core-loss and low-loss energy ranges to study the chemical compositional variation at the back surface of CdTe layers and along GBs intersecting the back surface. Three sample stacks of CdTe thin films (ITO/MZO/CdS/CdTe) are used in this comparative study. Two samples are Br:MeOH etched at the back surface of CdTe to create the Te back layer. After etching, a ZnTe layer is deposited at the back surface. This sample is used in the study as ZnTe is commonly deposited at the back surface of CdTe after bromine etching to create an electron-reflector layer. Finally, to ensure that the changes in chemical composition observed at the back surface of CdTe is an artifact of etching and not due to CdTe film growth, a third sample (ITO/MZO/CdS/CdTe/Te) deposited by vacuum deposition is used. This sample did not undergo any etching instead of a 30nm layer of Te is deposited at the back surface of CdTe.

Figure 1 shows the STEM EELS chemical maps (Cd and Te) of a GB at the back surface of bromine etched lamella from a cell with layer structure ITO/MZO/CdS/CdTe. In the Cd compositional map (Fig. 1b), the back surface and the GB region have relatively low Cd CL-EELS counts as compared to the grain bulk region on either side of the boundary while the same region has higher Te CL-EELS counts (Fig. 1c). This chemical variation shows that while the GB is poor in Cd, there is a higher concentration of Te in this region as compared to the bulk of

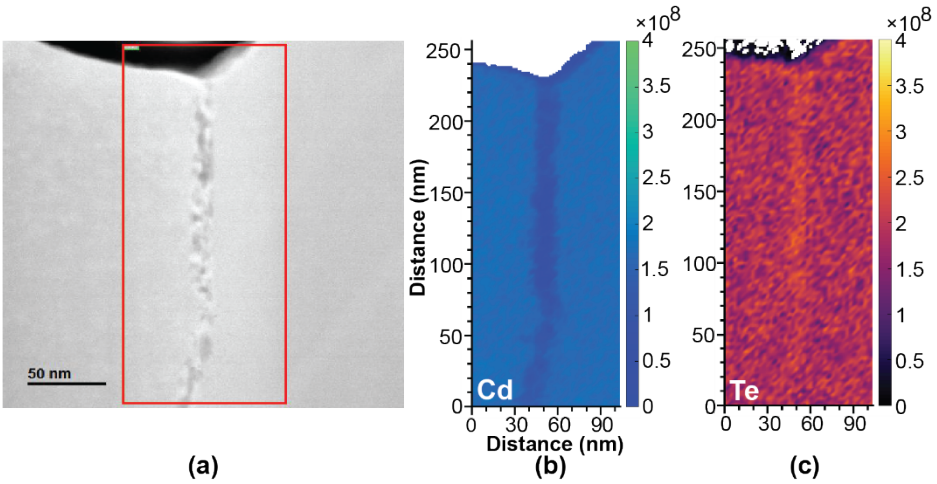

Figure 1. STEM EELS chemical map of a bromine etched back surface of of BrMeOH etched Glass/ITO/MZO/CdS/CdTe lamella. (a) HAADF STEM image of back surface of CdTe. (b) Cd, and (c) Te EELS chemical maps of the highlighted region in (a) showing Cd poor and Te rich grain boundary. Colorbar in units of atoms/nm^2.

the grain. The lack of Cd implies that after etching the sample with Br:MeOH, Cd^{2+} is selectively removed from the GB leaving behind a region that has a relatively higher concentration of Te. We believe that the GB exhibit excess Te as compared to the grain interior as a result of film growth conditions. This selective removal of Cd reduces the atomic density of the GB relative to the grain interior in the etch affected area. This low-density region shows up as darker GB regions in the HAADF-STEM image (Fig. 1a).

Figure 2 is the STEM-EELS chemical map of a GB region of Br-etched CdTe back surface from a cell with a layer structure ITO/MZO/CdS/CdTe/ZnTe. The ZnTe layer was deposited at the back after the Br:MeOH etching. Figure 2 d,e, and f are the HAADAF STEM image, Cd and Te EELS compositional maps, respectively, approximately 1 µm deep into the same GB. The chemical maps show that the GB region is deficient in Cd (Fig 2 b, d) and has higher Te (Fig 2 c, e) as compared to the adjacent grain bulk regions. Additionally, some regions in the GB are found to be devoid of Cd while very high in Te content compared to the grain interior. These pockets of no detectable Cd and high Te in the GB indicates that the etching process completely

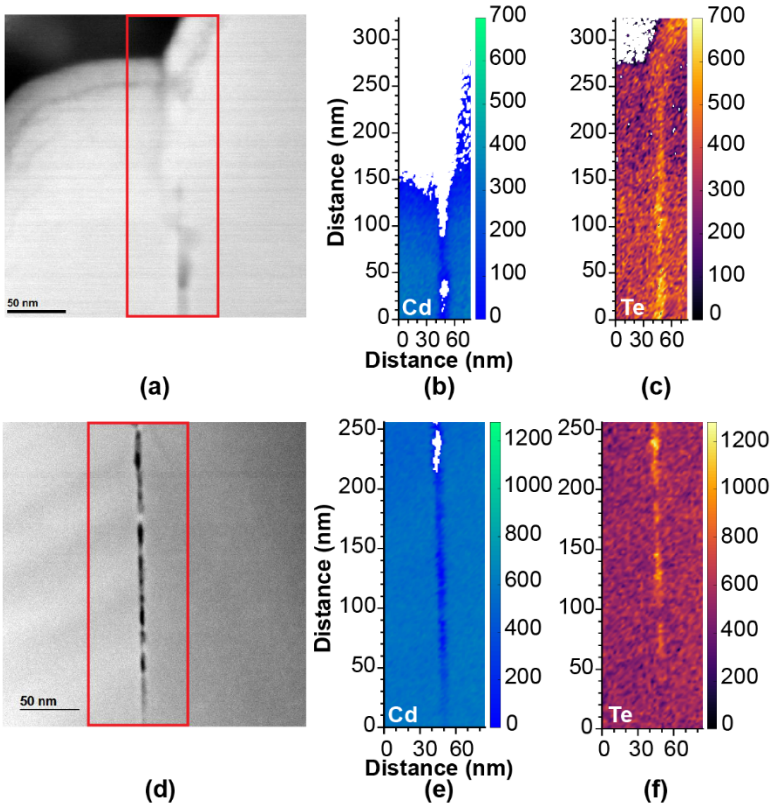

Figure 2. (a) HAADF STEM image of back surface of BrMeOH etched Glass/MZO/CdS/CdTe:ZnTe, (b) Cd, and (c) Te EELS chemical maps of the highlighted region in (a). (d) HAADF STEM image of same GB approximately 1 µm deeper into the sample (e) Cd and (f) Te EELS chemical maps of the highlighted region in (d). The grain boundary is Cd depleted and rich in Te. White regions in the chemical maps are areas where the Cd and Te signal was below background EELS level. Colorbar in units of atoms/nm^2.

removes Cd^{2+} ions from the structure leaving behind Te. Observation of higher Te concentration, in the GB compared to the grain interior region, this deep into the CdTe layer shows the extent of etching on GBs near the CdTe back surface.

Figure 3 compares the core loss spectrum of the GB region with that of the spectrum in the grain interior region. The normalized spectra in Figure 3b show that the signal from the GB region starts to rise at the onset of the Te M edge and there is a negligible signal response at the Cd M edge. This absence of the Cd M edge indicates that the Cd signal was not detected above the EELS background level in this region of the GB. This observation warrants further

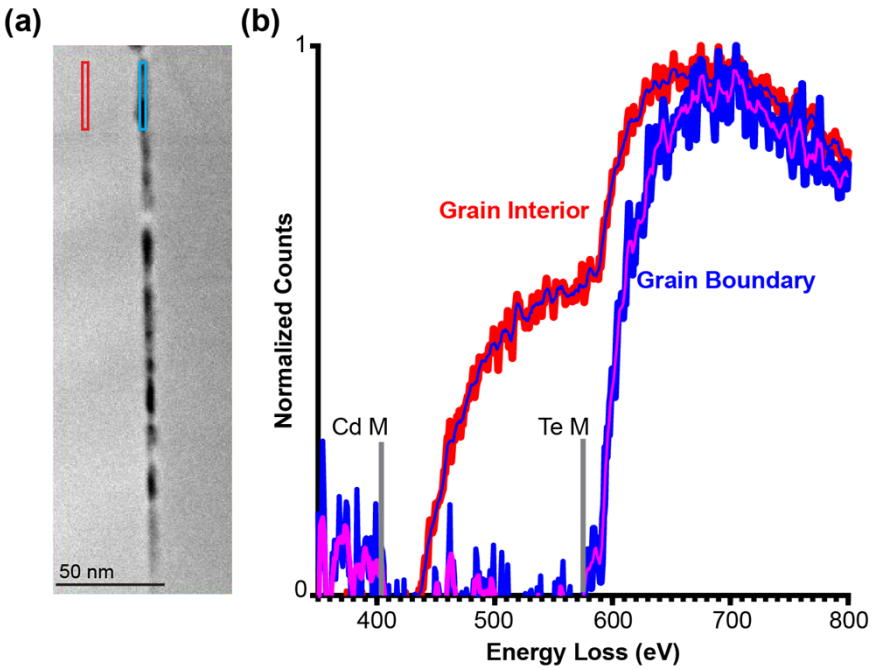

Figure 3. (a) HAADF STEM image of back surface of BrMeOH etched Glass/MZO/CdS/CdTe:ZnTe. (b) Integrated normalized core-loss EEL spectra of grain interior and grain boundary region showing no detectible Cd in the grain boundary region. Cd $M_{4,5}$ and Te $M_{4,5}$ onset lines are also shown on the energy loss axis.

investigation into the nature of the Te in the GB region; is it a region of highly Cd-poor CdTe, or is it a region of elemental Te?

In order to determine whether the higher concentration of Te observed at the GB is pure Te (Te bonded to Te) or a region CdTe with extreme Cd vacancies (Cd-poor CdTe), it is crucial to investigate the valence state of the high Te concentration observed in the GB region. Valence low loss spectral imaging was performed over the same region as in Figure 2. V-EELS spectra were collected at each pixel spanning from the Pt top layer through the CdTe bulk region. The spectra shown in Figure 4a were utilized as reference spectra for the Pt top layer, CdTe bulk region, and elemental Te. Then, the spectrum from each pixel was analyzed to determine the principal components. Individual weighted components were extracted by multiple linear least square (MLLS) fitting, where each spectrum was normalized and fitted with scaling coefficients adding up to one at each pixel forming maps of each of the phase components. Figure 4 shows

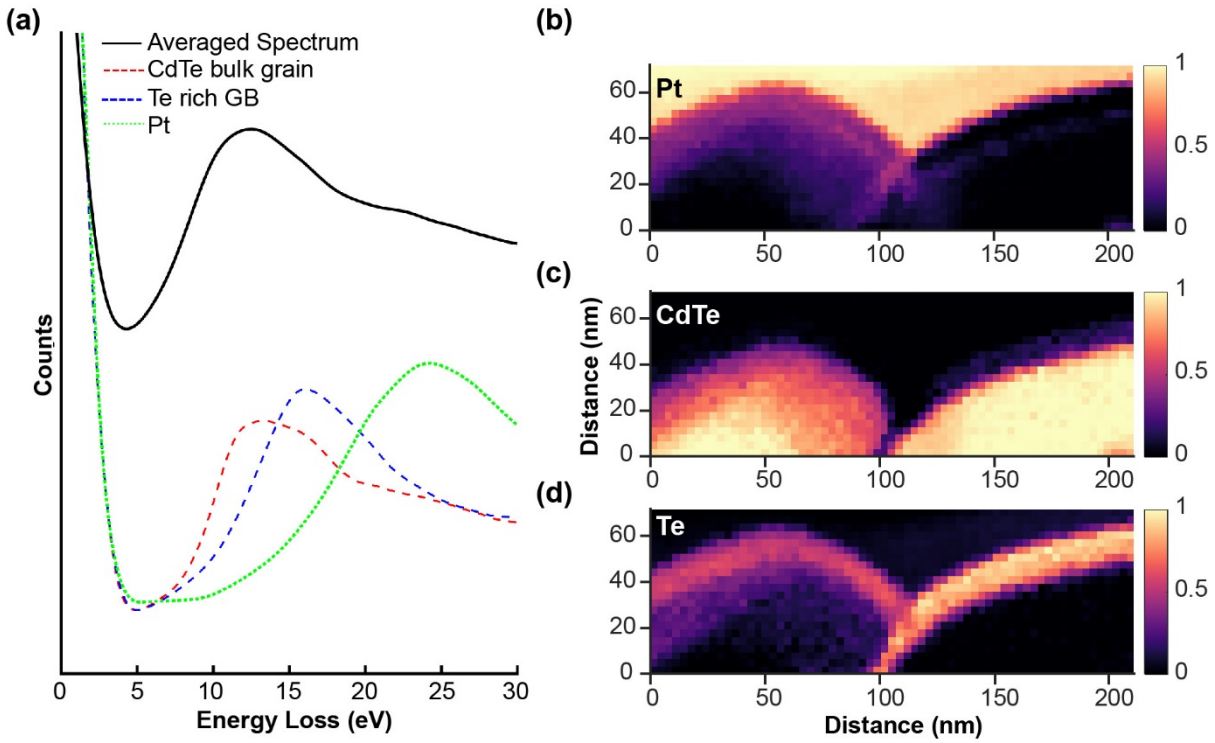

Figure 4. Component maps extracted from low-loss valence EELS spectral maps. (a) is MLLS fit of the three components (Pt, CdTe and Te) adding up to the averaged spectra (b) Pt top metal layer (c) CdTe bulk grain and (d) Te rich layer at the near back surface region of bromine etched Glass/ITO/MZO/CdTe:ZnTe film. Color bars show the fit coefficients of each component respectively.

these coefficient maps for the Pt (Fig 4 b), CdTe bulk (Fig 4 c), and Te GB (Fig 4 d) components. These maps reveal that the back surface of CdTe is Te rich with no CdTe and with minimal overlap of the Pt deposited layer. Principle component maps using the CdTe bulk grain and elemental Te spectra were also extracted along the same GB approximately 1 μm deep into the CdTe layer and are shown as Figure 5 a, b, respectively. The Te component map (Fig 5 b) shows that, even at this depth (~1 μm) from the back surface into the film, some regions of the GB have elemental Te with no detectible Cd. The fact that some GB regions correlate strongly with elemental Te component spectrum and not CdTe component demonstrates that these GB regions have elemental Te. It is also observed that only some regions of the etch affected area of

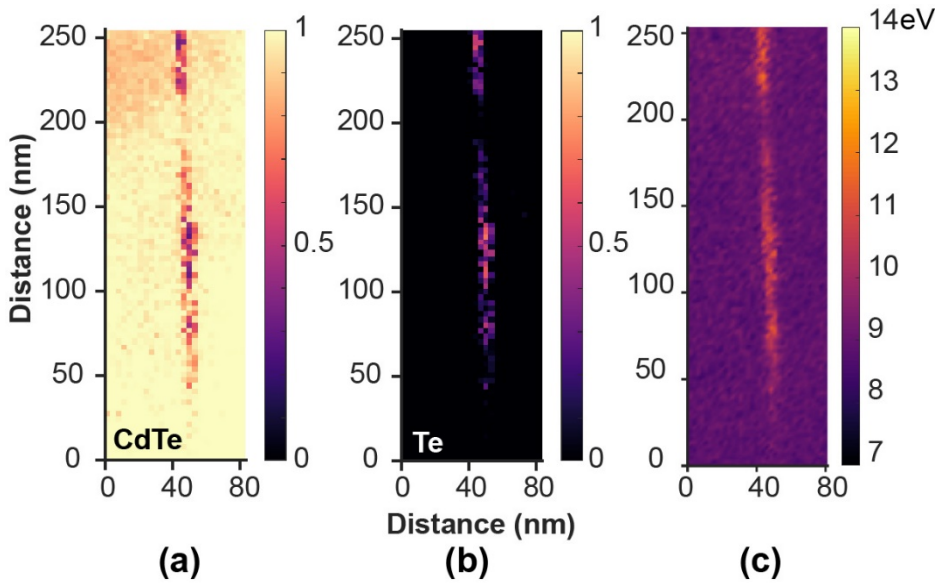

Figure 5. Component maps extracted from low loss valence EELS spectral maps for components (a) CdTe bulk grain, (b) elemental Te components respectively of the same GB as Figure 4 approximately 1 µm deeper in the sample. (c) shows imaginary part of the refractive index extracted from the low-loss valence EELS by Kraimer-Kronig analysis.

the GB is elemental Te. Therefore, the etch affected region of the GB has both Cd-poor CdTe as well as regions of elemental Te.

V-EELS spectra at each pixel was processed and KK analysis was performed to correlate the observed chemical changes at GB with the measured loss function (complex dielectric function). The required steps to perform the analysis included aligning to the zero-loss energy, minimizing plural scattering with the measured zero-loss peak, and tabulating the zero-loss full-width half maximum (FWHM) at each pixel.[45] Following KK analysis, the real and imaginary parts of the dielectric function were recorded at each point. Elemental Te, stoichiometric CdTe, and CdTe containing different concentrations of stoichiometry-changing point defects will all exhibit differences in their valence electron structure, thus resulting in shifts in their bulk plasmon spectra. Mapping the plasmon peak and comparing these peak positions with standard peaks recorded in EELS databases of the corresponding elements or compounds would point towards the bonding nature of the corresponding elements at each pixel. There is a direct correlation at

the GB region of the Te rich GB (Fig 5b) and the change in the bulk volume plasmon peak position (Fig 5c). Additionally, comparing to reference elemental Te spectra, the shift to higher energy is consistent with the presence of elemental Te. Experimentally measured V-EELS spectra published in the reference Gatan EELS Atlas database for elemental Te shows a reference peak at ~17 eV, whereas for CdTe the peak is centered at ~10.5 eV.[52] These reference spectra in the Gatan EELS Atlas were not minimized for plural scattering or analyzed with KK analysis, however, performing the same analysis on these reference spectra place the Te plasmon peak at the same energy (14 eV as shown in Fig 5c). This evidence validates our earlier hypotheses that the etching process not only produces a thin Te layer across the back surface but also converts CdTe to elemental Te in the near back-surface region of grain boundaries, sometimes extending as deep as 1 μm (nearly 33% into the film towards the front junction).

To thoroughly explore the issue of whether or not we can distinguish V-EELS spectra from Te-rich CdTe, Cd-poor CdTe, and elemental Te, we computed the bulk plasmon spectra using all-electron density functional theory (DFT). Figure 6 compares a representative experimental V-EELS spectrum from a Te-rich GB region with computed spectra for elemental Te, and CdTe containing various densities of Cd vacancies and Te interstitials. We note that these V-EELS spectra are sensitive to the area density of atoms but are rather insensitive to the crystallographic locations of atoms. Thus, we have confidence that any differences in the exact location and structure of atoms in the computed and experimental materials would not change the overall conclusions. The simulated spectra were smeared using a 1 eV Gaussian window to match our experimental parameters. The simulated spectra exhibit a monotonic shift in the peak position to higher energy going from stoichiometric CdTe to defective structures with a higher Te:Cd ratio,

to elemental Te. The computed spectra for pure Te has the best match with the experimental data, thus also supporting the hypothesis of etching-induced conversion to elemental Te.

In our prior work using STEM-based EDS, the x-ray generation and interaction volume were sufficiently large that x-rays from the adjacent CdTe grains were contained in the data, making it challenging to accurately determine whether the high concentration of Te observed in GBs is a region of Cd-poor CdTe or elemental Te. Additionally, comparing measured Te:Cd ratio in the chemical maps is not sufficient to distinguish elemental Te from stoichiometric CdTe. A region of Cd-poor CdTe and a region of high Te would both yield a Te:Cd ratio greater than one, making it impossible to determine the valence nature of the Te in the GB regions. Here using

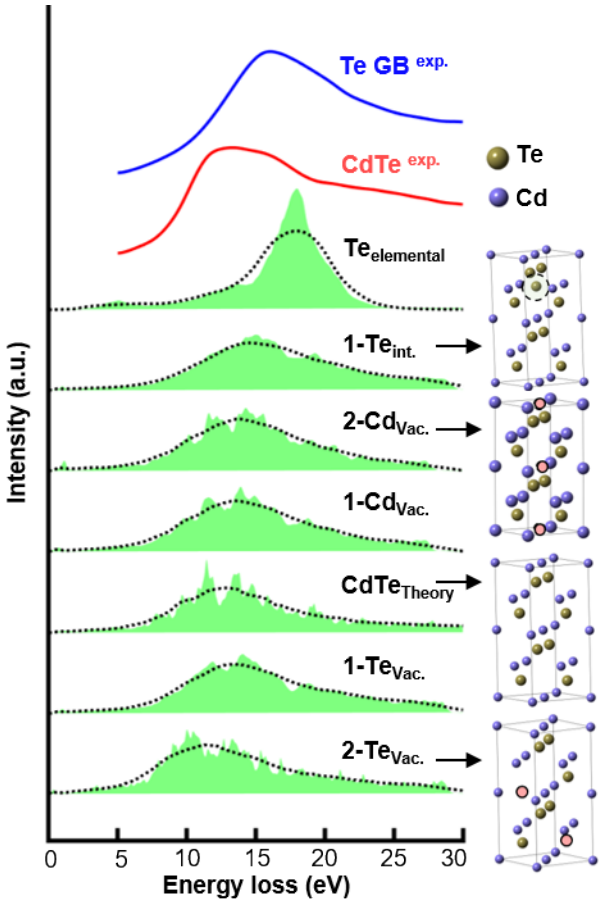

Figure 6. Comparison of theoretical EEL spectra obtained by DFT simulations of various defect conditions from stoichiometric CdTe with the experimental spectra of the components CdTe bulk grain and Te rich grain boundary respectively.

EELS, the smaller lateral resolution allows the presence of elemental Te in the affected regions of the GB to be determined conclusively. We conclude that the composition more closely resembles elemental Te than any defective CdTe and thus its chemical, electronic, and optical properties should also be expected to resemble elemental Te more closely. We cannot comment on whether or not the elemental Te in the GB is doped. However, its narrow bandgap of 0.33 eV (barely larger than the detailed balance mandated difference between E_g and V_{oc}) and high radiative recombination coefficient (~10^{-8} cm^3/s) ensure that the quasi-Fermi levels will remain very closely separated within Te regions turning the affected GB regions into an extension of the back contact.

To ensure that the Te rich GB regions are not formed during CdTe film deposition or $CdCl_2$ annealing processes but rather as a side-effect of the Br:MeOH etching, another lamella from the film stack (ITO/MZO/CdS/CdTe/Te) was analyzed. Instead of using etching to create a Te layer, a 30 nm Te layer was evaporated on top of the CdTe film. Figure 7 shows the STEM EELS chemical map for a GB region near the back surface of this film stack. In Figs. 7(b and c), the

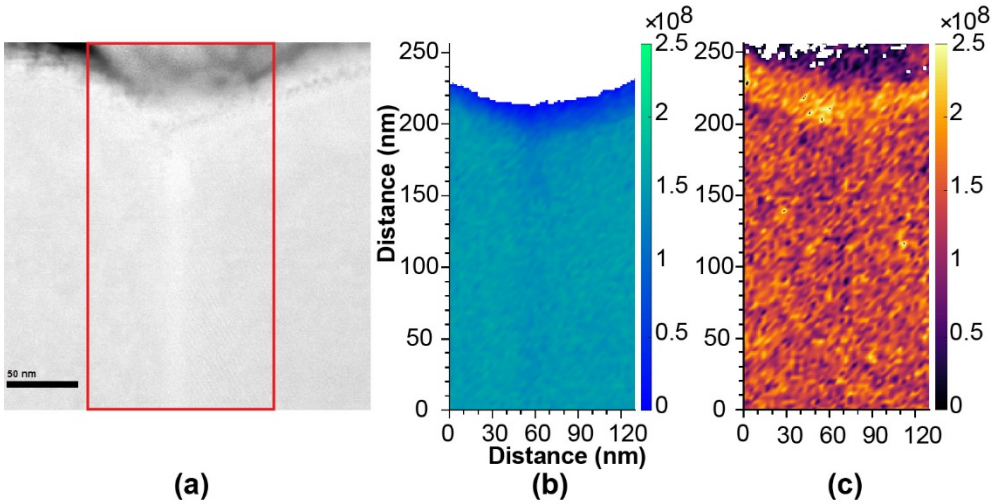

Figure 7. (a) HAADF STEM image of back surface of an unetched Te deposited Glass/ITO/MZO/CdS/CdTe, (b) Cd and (c) Te EELS chemical maps of the highlighted region in (a). No phase change of the GB is observed. Colorbar in units of atoms/nm^2.

GBs have barely-discernable contrast change indicating lower Cd concentration in the GB and even slighter hints of lower Te concentration. Both are only slightly above the to the signal fluctuation levels in the grains, with this statistical noise level being higher for the Te data. The STEM HAADF data also shows a brighter contrast in the GB, which is an imaging artifact due to the thickness of the TEM lamella. Thus, the only justifiable statement we can make about the composition of this GB is that there is no appreciable observable change in the stoichiometry of the GB. The Te chemical map (Fig 7 c) of this lamella shows a Te back surface but shows no detectable changes in Te composition along the GB region as compared to the adjacent grain interior regions. This lack of excess Te in the GB region indicates that the GB retains the same CdTe composition as the neighboring grains. Therefore, the evaporative deposition of Te at the back surface of CdTe preserves GB homogeneity while the high Te concentration found in GBs of the Br:MeOH etched films are due to the etching process and not an artifact of CdTe thin-film growth.

We turn now to a discussion of context and implications of the finding that Cd-selective etching processes can convert regions of grain boundaries from CdTe to elemental Te. It is evident from crystallographic considerations that in a compound crystal like CdTe, the bonds cut by a single GB may vary across its surface area if the GB is not strictly planar. Thus it should be expected that optoelectronic properties such as doping, recombination velocity, and bandgap may also vary. Also, different GBs described by the same grain misorientation and coincident site lattice (CSL) description may exhibit different optoelectronic properties because their surfaces may cut different sets of bonds. These two phenomena arise because five degrees of freedom are required to completely describe the local position (down to atomic scale) and orientation of the GB surface as well as the relative orientations of the two grains comprising a

GB. Only the two angular variables describing the orientation of the lattice are obtained from each point in electron backscatter diffraction (EBSD). The position of a GB cannot be resolved at atomic resolution, given the relatively larger interaction volume for EBSD. Thus, only the relative rotation of the two lattices may be determined at a GB. The three "missing" variables are the inclination of the GB plane with respect to the surface and absolute position of the GB in the surface plane which cannot be resolved at atomic resolution except by scanning transmission electron microscopy (STEM). These considerations are analogous to discussions of optoelectronic properties along a curvilinear dislocation which will exhibit different screw and edge components and thus different properties along its line.

In our earlier work, we carried out benchmark-quality two-dimensional device simulations on a representative CdTe device structure with representative absorber thickness and lateral grain size. Although we did not carry out full sweeps of CdTe thickness, doping, and lifetime along with GB lateral spacing, intragap defect density and recombination activity, simple arguments about whether or not minority carriers can reach affected GB regions before recombining radiatively in CdTe can yield qualitative trends. First, unlike the case of intragap defect recombination at GBs, the conversion of the bandgap from that of CdTe (1.5 eV) to that of Te (0.33 eV) means that even radiative recombination will result in smaller quasi-Fermi level splitting resulting in Voc losses. As long as the absorber layer is thick enough that negligible photocarriers reach areas of lower bandgap or higher recombination near the back contact, recombination at or near the back contact will not have a significant effect on V_{OC} or efficiency. A reasonable criterion for the effects of recombination at regions of reduced bandgap or increased nonradiative recombination near the back contact remaining insignificant is that such regions should be at least three minority carrier diffusion lengths from the edge of the front

junction depletion region. If either minority carrier diffusion length increases (Fig 8 b) or thickness of the quasi-neutral region of the absorber decreases (Fig 8 c), these types of recombination including any induced at GBs will need to be minimized in order to allow high V_{oc} and efficiency. The importance of band structure and doping at the back contact and strategies such as minority carrier reflector layers or back surface fields have long been recognized from 1D device physics considerations.[4,5] However, our observations indicate that GBs affected by etching intersecting the back surface introduce at least 2D bandstructure changes. The same arguments for back surface fields and minority carrier reflectors could in principle be implemented within the etch-affected regions of GBs in order to mitigate effects. However, in our opinion, it is better to avoid their formation by avoiding Cd-selective etching processes. Just as for unpassivated grain boundary regions having a high effective recombination velocity, the lateral spacing of grain boundaries compared to both the Debye and minority carrier diffusion lengths will help to determine the severity of impacts. Larger grains, higher intragrain doping, and a reduced number density and recombination activity of intragap defect states will all mitigate any effects.

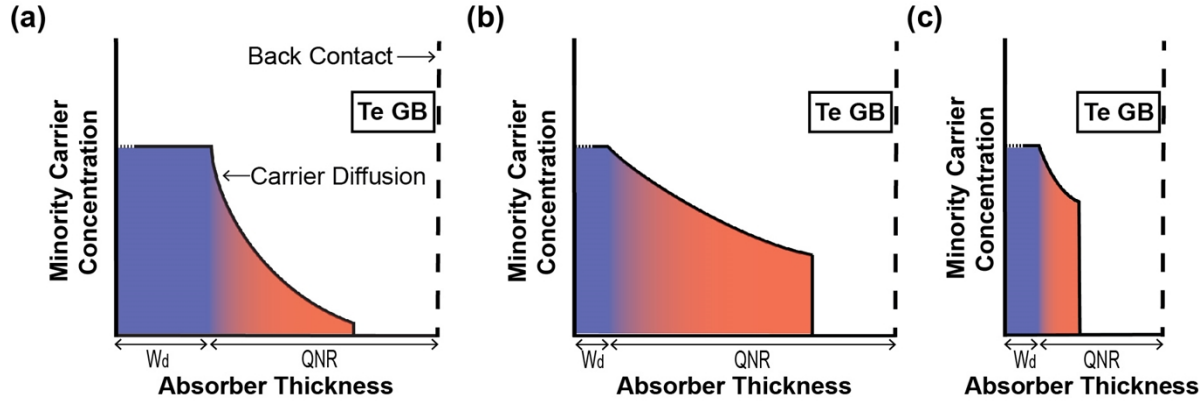

Figure 8. Illustration showing the effect of elemental Te in GB near the back surface of CdTe having (a) low minority carrier diffusion length, (b) large minority carrier diffusion length and (c) a lower than standard CdTe layer thickness.

CONCLUSION:

Chemical etching of the back-surface of CdTe leads to inhomogeneity within grain boundaries. The etching process affects the grain boundaries as deep as 1 μm into the absorber layer, nearly a third of the CdTe absorber layer. In addition to Cd-poor CdTe, the presence of elemental Te is confirmed in the etch affected region of grain boundary by correlating chemical compositions from CL-EELS with low-loss V-EELS and DFT based numerically predicted V-EELS spectra. Importantly, chemical etching leads to phase transformation within the grain boundaries from 1.5 eV CdTe to a lower bandgap 0.33 eV Te. Contrary to the currently accepted hypothesis that etching is beneficial to device efficiency, this observation of elemental Te as deep as 1 μm into the grain boundary from the back surface of CdTe is highly deleterious to extractable V_{OC} and device efficiency. However, additive deposition processes to form the Te back layer preserve the chemical composition of the grain boundary.

Recent and continued improvements in minority carrier lifetime, diffusion lengths and p-type doping in the absorber layer (CdTe) push towards creating thinner devices. The increased recombination due to the presence of lower bandgap Te in the grain boundaries of CdTe would lead to V_{OC} losses and thus limits the efficiency of CdTe TFPV devices. In light of this, it becomes crucial to avoid any form of wet-etching of CdTe back surface to aid in formation of an Ohmic back contact. Therefore, additive methods to create a Te back surface that preserves the chemical composition of the grain boundaries and is a better alternative to wet etching processes.

MATERIALS AND METHODS:

Sample Fabrication:

All samples used in this study are of superstrate architecture without the back metal contact. Borosilicate glass (Corning 7059) was used as the substrate. A brief etching in dilute hydrofluoric acid was used to clean the glass. A 300 nm indium doped tin oxide (ITO) layer was deposited on the glass by RF sputtering followed by a 100 nm layer of $Mg_xZn_{1-x}O$ (MZO). A 600-1000 Å of CdS was grown on the MZO layer by chemical bath deposition. A 3-5 μm thick layer of CdTe was deposited by sublimation. This sample is then annealed at 410 ºC in the presence of $CdCl_2$ to passivate the grain boundaries of the CdTe layer. Two of these samples were grown, and this is followed by a Br:MeOH etch (0.1% volumetric solution) for 10 seconds. On one of the samples, a 30 nm ZnTe layer is deposited by RF sputtering. The thickness of the CdTe absorber layer was ~3 μm.

To compare the etched process with that of a Te deposited back layer, another CdTe film stack is grown but without the Br:MeOH etching step. Instead, a 30nm Te layer was evaporated at the back surface.

Sample preparation for Scanning Transmission Electron Microscopy (STEM):

Electron transparent cross-sectional lamella were obtained from all the three processed samples using the standardized focused ion beam lift-out process. Following lift-out, a well-focused thinning of the lamella was performed (2 kV accelerating voltage and 12 pA beam current). Low accelerating voltage was used to clean the lamella of any residual material re-deposition and remove any damages from the lamella during the initial lift-out process (30 kV accelerating voltage). To further thin the samples without damaging the lamellas, a re-thinning was performed on the samples using Helium ion milling (Fischione 1040 NanoMill). Successive milling was done on the FIB lift-outs at 1 kV and 500 eV for 4 minutes on each side of the

lamella. The re-thinning was done to bring the thickness of the lamella closer to 60 nm while maintaining the surface integrity.

Scanning Transmission Electron Microscopy Characterization:

Annular dark-field images of the three lamellas were obtained using an aberration-corrected Nion UltraSTEM 100 microscope operated at 100 kV. The EELS measurements were done on the same system using Gatan Enfina EELS to obtain EELS spectrum images of the three lamellas at the back surface. The half convergence angle was set to 30 mrad, and the collection inner half-angle to 50 mrad. Before STEM characterization, the samples were baked overnight at 160 ºC in a vacuum. The STEM was operated in annular bright field and high angle annular dark-field (HAADF) imaging modes, with a calculated final probe diameter of 0.87 Å, based on the measured aberration coefficients. For quantifying the EELS chemical maps, Cd and Te component signals ($M_{4,5}$ edge) were extracted by fitting to the experimental spectra (in range of 350-800 eV) and deconvoluting the spectrum to account for the background signal, including removal of plural scattering effects due to thickness variations.

DFT calculations:

The addition and subtraction of Cd or Te effect on the joint density of states (DOS), low loss valence electron energy loss spectrum, and dielectric was predicted using first-principles density functional theory (DFT). Supercells were constructed on a 2 × 2 × 1 basis and sampled in reciprocal space using 4 × 4 × 4 k-point method, implemented in fully-relativistic all-electron linear augmented plane wave plus local orbital approach (LAPW+lo) employed in Wien2k version 18.2 (Release 7/17/2018).[53] Defect cells were constructed inside a primitive structure geometry where the addition or subtraction of Cd and Te atoms were constructed by hand and visualized inside the commercial software Crystal Maker version 9.2. With a varying amount of

Cd and Te content, the subsequent atomic coordinates were allowed to relaxed until self-convergence was achieved to less than 0.001 Rydbergs and 0.001 total charges forming an initial lattice structure of a = b = 6.629 Å and c = 13.2581 Å. The electron energy loss (EEL) spectra were calculated using the joint and TELNES3 submodules implemented in Wien2k, that readily converted the finite joint DOS to a comparable spectrum with an input broadening of 0.10 eV. The valence electron energy loss spectra were subsequently plotted and fitted using Matlab and the qualitative shifts in the spectra were compared with varying atomic content.

AUTHOR INFORMATION

Corresponding Author

*Email: sudhajit.misra@utah.edu.

ORCID ID:

Sudhajit Misra: 0000-0002-9099-842X

Michael A. Scarpulla: 0000-0002-6084-6839

Author Contributions

S.M. conceived the idea for this work. X.S and R.R U helped in STEM-EELS data collection. A.M, W.S. S, and C.S.F provided the samples for this study. S.M and J.A.A performed the data analysis. S.M and M.A.S directed the research. All authors discussed the data and commented on the manuscript.

Notes

The authors declare no competing financial interest.

ACKNOWLEDGMENTS:

This work at the University of Utah was supported in part by NSF, grant ECCS 1711885. The STEM-EELS characterization of the samples was performed at the Center for Nanophase Materials Sciences, which is a DOE Office of Science User Facility. The work supported in part through the INL Laboratory Directed Research & Development (LDRD) Program under DOE Idaho Operations Office Contract DE-AC07-05ID145142.

REFERENCES:

(1) Green, M. A.; Hishikawa, Y.; Dunlop, E. D.; Levi, D. H.; Hohl-Ebinger, J.; Ho-Baillie, A. W. Y. Solar Cell Efficiency Tables (Version 51). *Progress in Photovoltaics: Research and Applications* **2018**, *26* (1), 3–12. https://doi.org/10.1002/pip.2978.

(2) First Solar Achieves World Record 18.6 % Thin Film Module Conversion Efficiency https://investor.firstsolar.com/news/press-release-details/2015/First-Solar-Achieves-World-Record-186--Thin-Film-Module-Conversion-Efficiency/default.aspx (accessed Aug 28, 2019).

(3) Shockley, W.; Queisser, H. J. Detailed Balance Limit of Efficiency of P-n Junction Solar Cells. *Journal of Applied Physics* **1961**, *32* (3), 510–519. https://doi.org/10.1063/1.1736034.

(4) Ablekim, T.; Colegrove, E.; Metzger, W. K. Interface Engineering for 25% CdTe Solar Cells. *ACS Appl. Energy Mater.* **2018**, acsaem.8b01173. https://doi.org/10.1021/acsaem.8b01173.

(5) Liyanage, G. K.; Phillips, A. B.; Alfadhili, F. K.; Ellingson, R. J.; Heben, M. J. The Role of Back Buffer Layers and Absorber Properties for >25% Efficient CdTe Solar Cells. *ACS Appl. Energy Mater.* **2019**, *2* (8), 5419–5426. https://doi.org/10.1021/acsaem.9b00367.

(6) Kanevce, A.; Reese, M. O.; Barnes, T. M.; Jensen, S. A.; Metzger, W. K. The Roles of Carrier Concentration and Interface, Bulk, and Grain-Boundary Recombination for 25% Efficient CdTe Solar Cells. *Journal of Applied Physics* **2017**, *121* (21), 214506. https://doi.org/10.1063/1.4984320.

(7) Munshi, A. H.; Danielson, A. H.; Barth, K. L.; Gélinas, G.; Beaudry, J.; Sampath, W. S. Advanced Co-Sublimation of Low Bandgap CdSexTe1-XAlloy to Achieve Higher Short-Circuit Current. In *2018 IEEE 7th World Conference on Photovoltaic Energy Conversion (WCPEC) (A Joint Conference of 45th IEEE PVSC, 28th PVSEC 34th EU PVSEC)*; 2018; pp 0148–0152. https://doi.org/10.1109/PVSC.2018.8548272.

(8) Munshi, A. H.; Kephart, J.; Abbas, A.; Raguse, J.; Beaudry, J.-N.; Barth, K.; Sites, J.; Walls, J.; Sampath, W. Polycrystalline CdSeTe/CdTe Absorber Cells With 28 MA/Cm 2 Short-Circuit Current. *IEEE Journal of Photovoltaics* **2018**, *8* (1), 310–314.

(9) Munshi, A. H.; Kephart, J. M.; Abbas, A.; Shimpi, T. M.; Barth, K. L.; Walls, J. M.; Sampath, W. S. Polycrystalline CdTe Photovoltaics with Efficiency over 18% through

Improved Absorber Passivation and Current Collection. *Solar Energy Materials and Solar Cells* **2018**, *176*, 9–18.
(10) Ablekim, T.; Perkins, C.; Zheng, X.; Reich, C.; Swanson, D.; Colegrove, E.; Duenow, J. N.; Albin, D.; Nanayakkara, S.; Reese, M. O.; Shimpi, T.; Walajabad, S.; Metzger, W. K. Tailoring MgZnO/CdSeTe Interfaces for Photovoltaics. *IEEE Journal of Photovoltaics* **2019**, *9* (3), 888–892. https://doi.org/10.1109/JPHOTOV.2018.2877982.
(11) Fiducia, T. A. M.; Mendis, B. G.; Li, K.; Grovenor, C. R. M.; Munshi, A. H.; Barth, K.; Sampath, W. S.; Wright, L. D.; Abbas, A.; Bowers, J. W.; Walls, J. M. Understanding the Role of Selenium in Defect Passivation for Highly Efficient Selenium-Alloyed Cadmium Telluride Solar Cells. *Nat Energy* **2019**, *4* (6), 504–511. https://doi.org/10.1038/s41560-019-0389-z.
(12) Li, D.-B.; Song, Z.; Awni, R. A.; Bista, S. S.; Shrestha, N.; Grice, C. R.; Chen, L.; Liyanage, G. K.; Razooqi, M. A.; Phillips, A. B.; Heben, M. J.; Ellingson, R. J.; Yan,Y. Eliminating S-Kink To Maximize the Performance of MgZnO/CdTe Solar Cells. *ACS Appl. Energy Mater.* **2019**, *2* (4), 2896–2903. https://doi.org/10.1021/acsaem.9b00233.
(13) Zheng, X.; Kuciauskas, D.; Moseley, J.; Colegrove, E.; Albin, D. S.; Moutinho, H.; Duenow, J. N.; Ablekim, T.; Harvey, S. P.; Ferguson, A.; Metzger, W. K. Recombination and Bandgap Engineering in CdSeTe/CdTe Solar Cells. *APL Materials* **2019**, *7* (7), 071112. https://doi.org/10.1063/1.5098459.
(14) Yan, Y.; Albin, D.; Al-Jassim, M. M. Do Grain Boundaries Assist S Diffusion in Polycrystalline CdS/CdTe Heterojunctions? *Applied Physics Letters* **2001**, *78* (2), 171–173. https://doi.org/10.1063/1.1338969.
(15) Li, H.; X. Liu, X.; S. Lin, Y.; Yang, B.; M. Du, Z. Enhanced Electrical Properties at Boundaries Including Twin Boundaries of Polycrystalline CdTe Thin-Film Solar Cells. *Physical Chemistry Chemical Physics* **2015**, *17* (17), 11150–11155. https://doi.org/10.1039/C5CP00564G.
(16) Herndon, M. K.; Gupta, A.; Kaydanov, V.; Collins, R. T. Evidence for Grain-Boundary-Assisted Diffusion of Sulfur in Polycrystalline CdS/CdTe Heterojunctions. *Applied Physics Letters* **1999**, *75* (22), 3503–3505. https://doi.org/10.1063/1.125369.
(17) Durose, K.; Cousins, M. A.; Boyle, D. S.; Beier, J.; Bonnet, D. Grain Boundaries and Impurities in CdTe/CdS Solar Cells. *Thin Solid Films* **2002**, *403–404*, 396–404. https://doi.org/10.1016/S0040-6090(01)01518-8.
(18) Li, C.; Wu, Y.; Poplawsky, J.; Pennycook, T. J.; Paudel, N.; Yin, W.; Haigh, S. J.; Oxley, M. P.; Lupini, A. R.; Al-Jassim, M.; Pennycook, S. J.; Yan, Y. Grain-Boundary-Enhanced Carrier Collection in CdTe Solar Cells. *Physical Review Letters* **2014**, *112* (15). https://doi.org/10.1103/PhysRevLett.112.156103.
(19) Mendis, B. G.; Ramasse, Q. M.; Shalvey, T. P.; Major, J. D.; Durose, K. Optical Properties and Dielectric Functions of Grain Boundaries and Interfaces in CdTe Thin-Film Solar Cells. *ACS Appl. Energy Mater.* **2019**, *2* (2), 1419–1427. https://doi.org/10.1021/acsaem.8b01995.
(20) Terheggen, M.; Heinrich, H.; Kostorz, G.; Romeo, A.; Baetzner, D.; Tiwari, A. N.; Bosio, A.; Romeo, N. Structural and Chemical Interface Characterization of CdTe Solar Cells by Transmission Electron Microscopy. *Thin Solid Films* **2003**, *431–432*, 262–266. https://doi.org/10.1016/S0040-6090(03)00268-2.
(21) Guo, J.; Sen, F. G.; Mannodi-Kannakithodi, A.; Barnard, E. S.; Sampath, W.; Munshi, A.; Chan, M. K. Y.; Klie, R. F. Study of Effects of Cl and Se in CdSeTe Solar Cells Using

Scanning Transmission Electron Microscopy. *Microscopy and Microanalysis* **2019**, *25* (S2), 2150–2151. https://doi.org/10.1017/S1431927619011486.
(22) Mendis, B. G.; Bowen, L.; Jiang, Q. Z. A Contactless Method for Measuring the Recombination Velocity of an Individual Grain Boundary in Thin-Film Photovoltaics. *Appl. Phys. Lett.* **2010**, *97* (9), 092112. https://doi.org/10.1063/1.3486482.
(23) Visoly-Fisher, I.; Cohen, S. R.; Cahen, D. Direct Evidence for Grain-Boundary Depletion in Polycrystalline CdTe from Nanoscale-Resolved Measurements. *Applied Physics Letters* **2003**, *82* (4), 556–558. https://doi.org/10.1063/1.1542926.
(24) Major, J. D. Grain Boundaries in CdTe Thin Film Solar Cells: A Review. *Semicond. Sci. Technol.* **2016**, *31* (9), 093001. https://doi.org/10.1088/0268-1242/31/9/093001.
(25) Smith, S.; Zhang, P.; Gessert, T.; Mascarenhas, A. Near-Field Optical Beam-Induced Currents in CdTe/CdS Solar Cells: Direct Measurement of Enhanced Photoresponse at Grain Boundaries. *Appl. Phys. Lett.* **2004**, *85* (17), 3854–3856. https://doi.org/10.1063/1.1809271.
(26) Moseley, J.; Metzger, W. K.; Moutinho, H. R.; Paudel, N.; Guthrey, H. L.; Yan, Y.; Ahrenkiel, R. K.; Al-Jassim, M. M. Recombination by Grain-Boundary Type in CdTe. *Journal of Applied Physics* **2015**, *118* (2), 025702. https://doi.org/10.1063/1.4926726.
(27) Visoly-Fisher, I.; Cohen, S. R.; Gartsman, K.; Ruzin, A.; Cahen, D. Understanding the Beneficial Role of Grain Boundaries in Polycrystalline Solar Cells from Single-Grain-Boundary Scanning Probe Microscopy. *Advanced Functional Materials* **2006**, *16* (5), 649–660. https://doi.org/10.1002/adfm.200500396.
(28) Simonds, B. J.; Palekis, V.; Van Devener, B.; Ferekides, C.; Scarpulla, M. A. Surface Stoichiometry of Pulsed Ultraviolet Laser Treated Polycrystalline CdTe. *Journal of Applied Physics* **2014**, *116* (1), 013506. https://doi.org/10.1063/1.4887079.
(29) Misra, S.; Aguiar, J. A.; Sun, Y.; Devener, B. v; Palekis, V.; Ferekides, C. S.; Yoon, H. P.; Bermel, P.; Scarpulla, M. A. Observation and Implications of Composition Inhomogeneity Along Grain Boundaries in Thin Film Polycrystalline CdTe Photovoltaic Devices. *Advanced Materials Interfaces* **2019**, *6* (16), 1900152. https://doi.org/10.1002/admi.201900152.
(30) Niles, D. W.; Li, X.; Sheldon, P.; Höchst, H. A Photoemission Determination of the Band Diagram of the Te/CdTe Interface. *Journal of Applied Physics* **1995**, *77* (9), 4489–4493. https://doi.org/10.1063/1.359444.
(31) Sarlund, J.; Ritala, M.; Leskelä, M.; Siponmaa, E.; Zilliacus, R. Characterization of Etching Procedure in Preparation of CdTe Solar Cells. *Solar Energy Materials and Solar Cells* **1996**, *44* (2), 177–190. https://doi.org/10.1016/0927-0248(96)00053-0.
(32) Dharmadasa, I. M.; Thornton, J. M.; Williams, R. H. Effects of Surface Treatments on Schottky Barrier Formation at Metal/N-type CdTe Contacts. *Appl. Phys. Lett.* **1989**, *54* (2), 137–139. https://doi.org/10.1063/1.101208.
(33) Rimmaudo, I.; Salavei, A.; Artegiani, E.; Menossi, D.; Giarola, M.; Mariotto, G.; Gasparotto, A.; Romeo, A. Improved Stability of CdTe Solar Cells by Absorber Surface Etching. *Solar Energy Materials and Solar Cells* **2017**, *162*, 127–133. https://doi.org/10.1016/j.solmat.2016.12.044.
(34) Reese, M. O.; Perkins, C. L.; Burst, J. M.; Farrell, S.; Barnes, T. M.; Johnston, S. W.; Kuciauskas, D.; Gessert, T. A.; Metzger, W. K. Intrinsic Surface Passivation of CdTe. *Journal of Applied Physics* **2015**, *118* (15), 155305. https://doi.org/10.1063/1.4933186.

(35) Misra, S.; Pruzan, D. S.; Richey-Simonsen, L. R.; Wang, M.; Palekis, V.; Aguiar, J. A.; Gerton, J.; Ferekides, C.; Scarpulla, M. A. Mapping Carrier Lifetime Variations in Polycrystalline CdTe Thin Films Using Confocal Microscopy. In *2018 IEEE 7th World Conference on Photovoltaic Energy Conversion (WCPEC) (A Joint Conference of 45th IEEE PVSC, 28th PVSEC 34th EU PVSEC)*; 2018; pp 1925–1927. https://doi.org/10.1109/PVSC.2018.8548004.

(36) McCandless, B. E.; Dobson, K. D. Processing Options for CdTe Thin Film Solar Cells. *Solar Energy* **2004**, *77* (6), 839–856. https://doi.org/10.1016/j.solener.2004.04.012.

(37) Strevel, N.; Trippel, L.; Kotarba, C.; Khan, I. Improvements in CdTe Module Reliability and Long-Term Degradation through Advances in Construction and Device Innovation. *Photovoltaics International* **2013**, *22*, 66–74.

(38) Wolden, C. A.; Abbas, A.; Li, J.; Diercks, D. R.; Meysing, D. M.; Ohno, T. R.; Beach, J. D.; Barnes, T. M.; Walls, J. M. The Roles of ZnTe Buffer Layers on CdTe Solar Cell Performance. *Solar Energy Materials and Solar Cells* **2016**, *147*, 203–210. https://doi.org/10.1016/j.solmat.2015.12.019.

(39) Kurley, J. M.; Panthani, M. G.; Crisp, R. W.; Nanayakkara, S. U.; Pach, G. F.; Reese, M. O.; Hudson, M. H.; Dolzhnikov, D. S.; Tanygin, V.; Luther, J. M.; Talapin, D. V.;. Transparent Ohmic Contacts for Solution-Processed, Ultrathin CdTe Solar Cells. *ACS Energy Lett.* **2017**, *2* (1), 270–278. https://doi.org/10.1021/acsenergylett.6b00587.

(40) Salavei, A.; Menossi, D.; Piccinelli, F.; Kumar, A.; Mariotto, G.; Barbato, M.; Meneghini, M.; Meneghesso, G.; Di Mare, S.; Artegiani, E.; Romeo, A. Comparison of High Efficiency Flexible CdTe Solar Cells on Different Substrates at Low Temperature Deposition. *Solar Energy* **2016**, *139*, 13–18. https://doi.org/10.1016/j.solener.2016.09.004.

(41) Mahabaduge, H. P.; Rance, W. L.; Burst, J. M.; Reese, M. O.; Meysing, D. M.; Wolden, C. A.; Li, J.; Beach, J. D.; Gessert, T. A.; Metzger, W. K.;Garner, S., Barnes, T. M. High-Efficiency, Flexible CdTe Solar Cells on Ultra-Thin Glass Substrates. *Applied Physics Letters* **2015**, *106* (13), 133501. https://doi.org/10.1063/1.4916634.

(42) Cho, E.; Kang, Y.; Kim, D.; Kim, J. Post-Growth Process for Flexible CdS/CdTe Thin Film Solar Cells with High Specific Power. *Opt. Express, OE* **2016**, *24* (10), A791–A796. https://doi.org/10.1364/OE.24.00A791.

(43) Prospects for analyzing the electronic properties in nanoscale systems by VEELS - ScienceDirect https://www.sciencedirect.com/science/article/pii/S0304399107002410 (accessed Aug 31, 2019).

(44) Quantifying the low-energy limit and spectral resolution in valence electron energy loss spectroscopy - ScienceDirect https://www.sciencedirect.com/science/article/pii/S0304399112002148 (accessed Aug 31, 2019).

(45) Egerton, R. F. *Electron Energy-Loss Spectroscopy in the Electron Microscope*, 3rd ed.; Springer US, 2011.

(46) Aguiar, J. A. Atomic Scale Characterization of Materials Using Scanning Transmission Electron Microscopy. *Ph.D. Thesis* **2012**.

(47) Scott, J.; Thomas, P. J.; MacKenzie, M.; McFadzean, S.; Wilbrink, J.; Craven, A. J.; Nicholson, W. A. P. Near-Simultaneous Dual Energy Range EELS Spectrum Imaging. *Ultramicroscopy* **2008**, *108* (12), 1586–1594. https://doi.org/10.1016/j.ultramic.2008.05.006.

(48) Mizoguchi, T.; Miyata, T.; Olovsson, W. Excitonic, Vibrational, and van Der Waals Interactions in Electron Energy Loss Spectroscopy. *Ultramicroscopy* **2017**, *180*, 93–103. https://doi.org/10.1016/j.ultramic.2017.03.003.
(49) Meadows, H. J.; Regesch, D.; Thevenin, M.; Sendler, J.; Schuler, T.; Misra, S.; Simonds, B. J.; Scarpulla, M. A.; Gerliz, V.; Gütay, L.; Guillot, J., Dale P. J.. CuInSe2 Semiconductor Formation by Laser Annealing. *Thin Solid Films* **2015**, *582*, 23–26. https://doi.org/10.1016/j.tsf.2014.10.042.
(50) Meadows, H. J.; Misra, S.; Simonds, B. J.; Kurihara, M.; Schuler, T.; Reis-Adonis, V.; Bhatia, A.; Scarpulla, M. A.; Dale, P. J. Laser Annealing of Electrodeposited CuInSe2 Semiconductor Precursors: Experiment and Modeling. *J. Mater. Chem. C* **2017**, *5* (6), 1336–1345. https://doi.org/10.1039/C6TC03623F.
(51) Meadows, H. J.; Regesch, D.; Schuler, T.; Misra, S.; Simonds, B. J.; Scarpulla, M. A.; Gerliz, V.; Gütay, L.; Dale, P. The Importance of Se Partial Pressure in the Laser Annealing of CuInSe2 Electrodeposited Precursors. In *2014 IEEE 40th Photovoltaic Specialist Conference (PVSC)*; 2014; pp 0405–0408. https://doi.org/10.1109/PVSC.2014.6924944.
(52) Tellurium https://www.eels.info/atlas/tellurium (accessed Aug 26, 2019).
(53) Blaha, P.; Schwarz, K.; Sorantin, P.; Trickey, S. B. Full-Potential, Linearized Augmented Plane Wave Programs for Crystalline Systems. *Computer Physics Communications* **1990**, *59* (2), 399–415. https://doi.org/10.1016/0010-4655(90)90187-6.
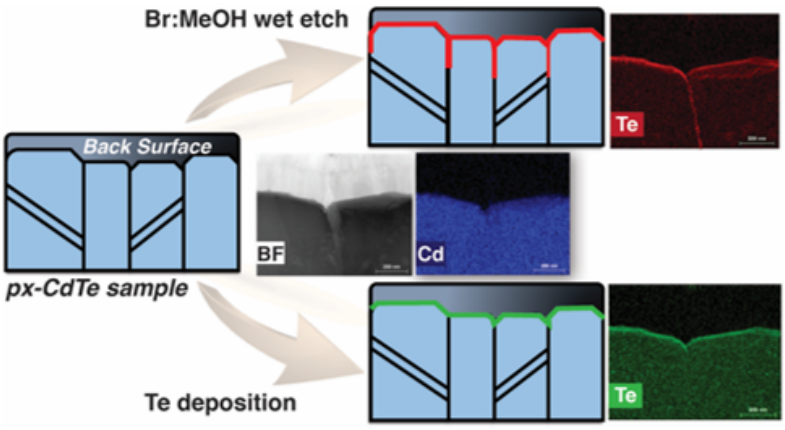
Table of Contents Figure: